American Mineralogist, Volume 106, pages 1980–1986, 2021

Tin isotopes via fs-LA-MC-ICP-MS analysis record complex fluid evolution in single cassiterite crystals

Peng Liu[1,†], Jingwen Mao[2,*], Bernd Lehmann[3], Stefan Weyer[4], Ingo Horn[4], Ryan Mathur[5], Fangyue Wang[6], and Zhenhua Zhou[2]

[1]School of Earth Sciences and Resources, Chang'an University, Xi'an 710054, China
[2]Ministry of Natural Resources (MNR) Key Laboratory of Metallogeny and Mineral Assessment, Institute of Mineral Resources, Chinese Academy of Geological Sciences (CAGS), Beijing 100037, China
[3]Mineral Resources, Clausthal University of Technology, 38678 Clausthal-Zellerfeld, Germany
[4]Institut für Mineralogie, Leibniz Universität Hannover, 30167 Hannover, Germany
[5]Juniata College, Huntingdon, Pennsylvania 16652, U.S.A
[6]Ore Deposit and Exploration Centre, School of Resources and Environmental Engineering, Hefei University of Technology, Hefei 230009, China

Abstract

Tin isotope geochemistry of cassiterite may allow for reconstructing the fluid evolution of tin ore deposits. Here, we present cathodoluminescence (CL) imaging, trace element, and in situ Sn isotope compositions of two cassiterite crystals from an early and a relatively late stage of ore formation of the Xiling vein-style Sn deposit, southeastern China, by femtosecond laser ablation multi-collector inductively coupled plasma mass spectrometry (fs-LA-MC-ICP-MS). Our results show that the early-stage cassiterite from a high-temperature feldspar-stable hydrothermal environment has core, mantle, and rim zones with a systematic decrease in $\delta^{124/117}Sn_{3161A}$ (relative to the Sn standard NIST 3161 A) from +0.38 ± 0.06‰ in the crystal core to –0.12 ± 0.06‰ (2 SE) in the mantle zone. This isotopic evolution, also paralleled by a decrease in Ta content by two orders of magnitude, suggests a fluid batch evolving toward isotopically lighter Sn. The very rim zone of this crystal has an intermediate tin isotope composition at about +0.05‰ $\delta^{124/117}Sn_{3161A}$, combined with elevated Ta, suggestive of a second fluid batch. The late-stage cassiterite crystal from a muscovite-stable hydrothermal environment has a core with an evolved Sn isotope composition at about –0.15‰ $\delta^{124/117}Sn_{3161A}$ combined with low Ta, and a rim with heavier Sn isotope compositions up to +0.30 ± 0.08‰ $\delta^{124/117}Sn_{3161A}$ and higher Ta contents. As for the early-stage crystal, two different fluid batches must be involved in the formation of this crystal. Our pilot study highlights the advantage of spatially resolved analysis compared to conventional, solution Sn-isotope analysis of bulk cassiterite crystals. The Sn isotope variations at the microscale reveal the complexity of cassiterite crystal growth by a combination of closed- and open-system fluid evolution and isotope fractionation.

Keywords: Xiling, tin ore deposit, cassiterite, trace-element mapping, in-situ Sn isotope

Introduction

Cassiterite [SnO_2] is the most important ore mineral in tin deposits and can form in magmatic and hydrothermal systems over broad *P-T-X* conditions (Jackson and Helgeson 1985a, 1985b; Heinrich 1990). Individual cassiterite crystals commonly show distinct zonation patterns in optical (Cheng et al. 2019), cathodoluminescence (CL) or backscatter images, and corresponding microchemical features, indicating changes in physico-chemical conditions during their growth process.

Tin has 10 stable isotopes, and investigations of the Sn isotope composition revealed ‰-level variations in natural materials, including meteorites (Creech and Moynier 2019) and Sn ore deposits (Haustein et al. 2010; Yamazaki et al. 2013; Schulze et al. 2017; Yao et al. 2018); and even more significant variations between magmatic rocks from the Earth and the Moon (Wang et al. 2018, 2019a). The first MC-ICP-MS reconnaissance studies by Haustein et al. (2010) and Yamazaki et al. (2013) observed significant differences in tin isotope composition among cassiterite samples from different localities. The latter study identified a range in $\delta^{124/120}Sn_{SPEX}$ of –0.44 to +0.38 (corresponding to $\delta^{124/120}Sn_{3161A}$ of +0.11 to +0.93) in cassiterite from Eastern Asia. A similar range was also observed by Brügmann et al. (2017) in cassiterite from European and Rwanda tin ore deposits. Yao et al. (2018) showed that the tin isotope composition of cassiterite from global tin deposits (with $\delta^{124/116}Sn_{3161A}$ of 0.48 ± 0.62‰, 1σ) is consistently less fractionated than paragenetically later stannite [Cu_2FeSnS_4] formed at a lower temperature (with –1.47 ± 0.54‰, 1σ). This isotopic shift has been attributed to the oxidation of Sn^{2+} in solution and concomitant precipitation of heavy-Sn-enriched cassiterite (SnO_2 with Sn^{4+}), resulting in residual dissolved Sn with lighter isotopic composition, which is expressed in the more negative $\delta^{124/115}Sn$ values of later-formed stannite. Theoretical and experimental studies suggest that Sn isotope fractionation can be caused by redox reactions and liquid-

* E-mail: jingwenmao@263.net
† Orcid 0000-0001-6396-0525

vapor phase separation (Polyakov et al. 2005; Wang et al. 2019b; She et al. 2020). However, previous empirical studies focused on Sn-isotope determinations of bulk samples by solution chemistry and MC-ICP-MS analysis. Up to now, in situ Sn isotope measurements were only reported by Schulze et al. (2017), comparing solution MC-ICP-MS to in situ measurements using femtosecond laser-ablation multi-collector inductively-coupled mass spectrometry (LA-MC-ICP-MS). Spatially resolved methods, including in situ Sn-isotope analysis of cassiterite, may provide high-resolution details that would remain unrecognized in solution isotope analysis of bulk minerals or rocks.

Here, we combine CL, trace element, and in situ Sn isotopes to track changing fluid compositions, as recorded in concentrically zoned cassiterite crystals. We selected two cassiterite crystals from the hydrothermal vein-style Xiling tin deposit, southeastern China. Our results indicate compositional heterogeneity at the sub-millimeter scale in terms of trace elements and tin isotope composition, which reveal a more complex fluid evolution than expected by analytical bulk mineral techniques. The features of the tin isotope fractionation can be attributed to fractional crystallization of cassiterite, both in relatively closed-system and open-system environments.

Geological background and samples

The hydrothermal vein-style Xiling tin deposit is located in eastern Guangdong Province, southeastern China (Online Materials[1] Fig. OM1). The tin mineralization is predominantly hosted in Upper Jurassic volcanic/subvolcanic rhyolite (Fig. 1), and the U-Pb age of cassiterite of 146–147 Ma suggests a hidden granite intrusion as the source of the hydrothermal system (Liu et al. 2018, 2020). There are two main ore types in the Xiling deposit: (1) veins of cassiterite + feldspar ± quartz, and (2) veins of cassiterite + quartz ± muscovite (Figs. 2a–2d). These two mineral assemblages represent early-stage (I) cassiterite related to potassic alteration and relatively late-stage (II) cassiterite related to phyllic alteration. Two-phase aqueous fluid inclusions from stage 1 have a salinity around 15 wt% NaCl eq. and homogenization temperatures of 350–380 °C, while the two-phase aqueous fluid inclusions from stage 2 have a low salinity ≤5 wt% NaCl eq. and homogenization temperatures of 250–280 °C (Liu et al. 2020). We selected two cassiterite crystals, hereafter referred to as early-stage cassiterite and late-stage cassiterite (samples 17XL05 and 14XL01, respectively), which were prepared as thick polished sections for cathodoluminescence imaging, LA-ICP-MS trace-element (single-spot and mapping) and in situ Sn isotope analysis (see analytical method for SEM-CL and trace-element analysis in Appendix 1[1]). Early-stage cassiterite occurs mostly as stout prismatic, euhedral to subhedral crystals, 3–10 mm across in feldspar-quartz veins (Fig. 2c). Late-stage cassiterite is found as prismatic euhedral crystals that are 1 to 4 mm across in muscovite-bearing quartz veins (Fig. 2d).

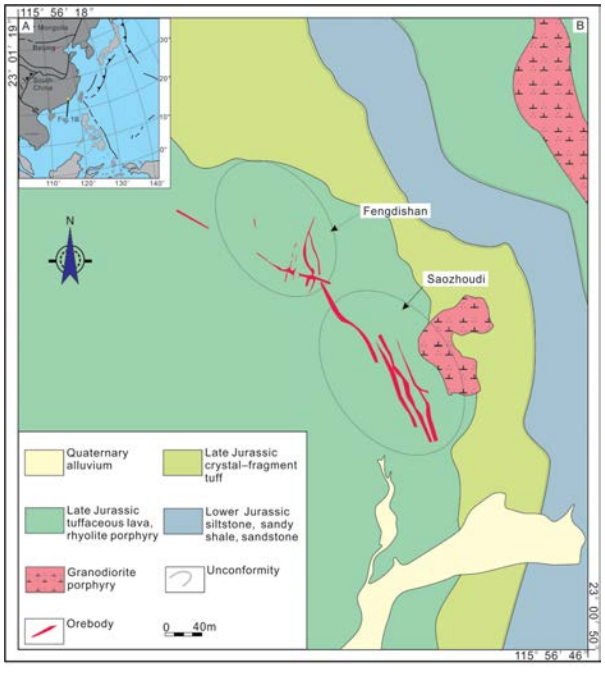

Figure 1. Geological map of the Xiling deposit (Liu et al. 2018). Ore bodies are projected to the surface. (Color online.)

Analytical method for Sn isotope analysis

In situ cassiterite Sn isotope analyses of cassiterite were performed at the Leibniz Universität Hannover (Germany) by using a MC-ICP-MS (Thermo-Finnigan Neptune Plus) instrument connected to an in-house built femtosecond laser ablation system based on a Solstice (Spectra Physics, U.S.A.) regenerative amplified femtosecond laser and an UP-XP laser stage system for beam delivery (New Wave Research). Detailed information about the laser system can be found in Horn and von Blanckenburg (2007) and Schulze et al. (2017). Tin isotope analyses were performed as outlined in Schulze et al. (2017) (and using the same instruments). As detailed in Schulze et al. (2017), mass bias was corrected in this study by sample-standard bracketing using a rod of pure Sn (99.9% Sn) (Halsbrücke, Germany) as bracketing standard. Furthermore, an Sb mass bias monitor was introduced by solution nebulization. A potential mass interference from ^{124}Te on ^{124}Sn was monitored by simultaneous analyses of ^{125}Te. As the cassiterite crystals investigated in this study were generally heterogeneous, it was not possible to determine a value for the precision or even "accuracy" of the in situ analyses, e.g., based on replicate analyses. The precision and accuracy of the in situ analyses, judged on agreement with solution analyses, was previously determined by Schulze et al. (2017). They analyzed several cassiterite crystals (which were previously homogenized by melting) by both solution MC-ICP-MS and fs-LA-MC-ICP-MS. With this approach, they could determine a precision (for replicate laser spot analyses) and estimate an accuracy (more precisely, agreement with solution analyses) of better than 0.1‰ (at 95% confidence level). This precision is considered as overall uncertainty for reported Sn isotope ratios in this study. Internal precisions of individual analyses, as reported in Table 1, were generally <0.1‰ (2 SE) and are also shown as error bars in Figures 3 and 4. The Sn isotope compositions are given as variation in parts per mil (‰), using the δ notation. They are initially determined as $\delta^{124/117}$Sn values relative to the Sn rod:

$$\delta^{124/117}Sn_{rod} = \{[(^{124}Sn/^{117}Sn)_{sample}/(^{124}Sn/^{117}Sn)_{Sn\ rod}] - 1\} \times 1000.$$

The Sn rod standard was measured after every 1–2 sample analyses for drift monitoring. The isotope composition of the Sn rod is indistinguishable from that of the SPEX CertiPrep CLSN2-2Y standard (Schulze et al. 2017). Yamazaki et al. (2013) and Brügmann et al. (2017) cross-calibrated Sn SPEX CertiPrep CLSN2-2Y relative to NIST 3161A and found: $\delta^{124/117}Sn_{3161A} = \delta^{124/117}Sn_{SPEX} + 0.55$. Combining the calibration of our Sn rod relative to SPEX (Schulze et al. 2017) and the calibration of SPEX relative to NIST 3161A (Yamazaki et al. 2013) and Brügmann et al. (2017), we converted all isotope compositions determined in this study relative to Sn rod to δ values relative to NIST 3161A by applying the following equation:

$$\delta^{124/117}Sn_{3161A} = \delta^{124/117}Sn_{rod} + 0.55.$$

We used this conversion to facilitate comparison to previously published values, e.g., for Bulk Silicate Earth (Wang et al. 2018) and other studies on ores (Yao et al. 2018).

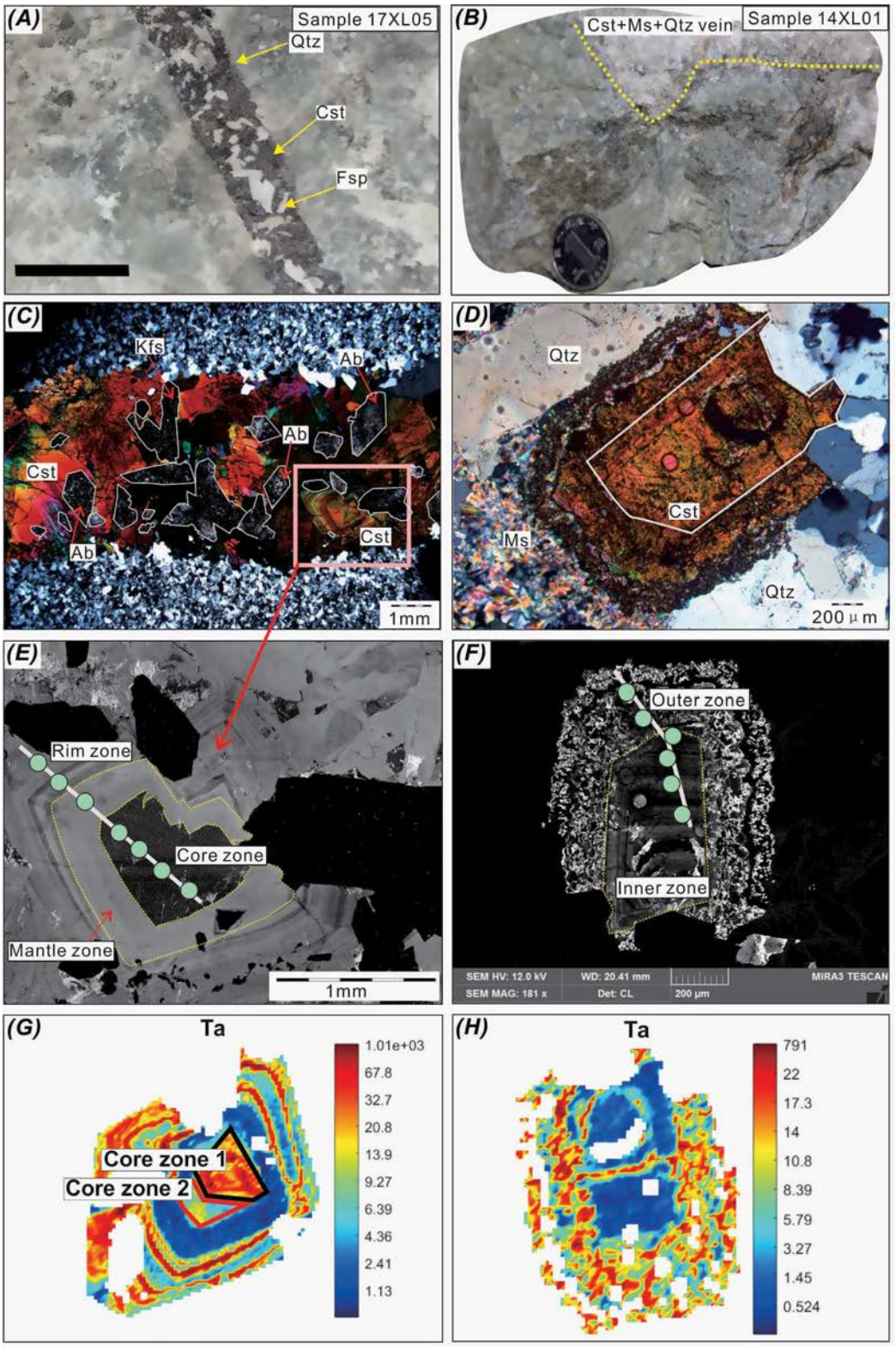

Figure 2. (**a** and **b**) Photographs and CL image of the ores from Stage I (potassic; sample 17XL05) and II (phyllic; sample 14XL01). (**c** and **d**) Photomicrographs of cassiterite from Stage I and II under crossed polarized light. (**e** and **f**) CL images of the two cassiterite crystals; the boundary between core and rim zones is marked by a yellow line. (**g** and **h**) Ta elemental mapping of the two cassiterite crystals. Abbreviations: Ab = albite; Cst = cassiterite; Ms = muscovite; Kfs = K-feldspar; Qtz = quartz. (Color online.)

Table 1. fs-LA-MC-ICP-MS isotope data for the two cassiterite samples (‰); $\delta^{124/117}Sn_{3161A} = \delta^{124/117}Sn_{rod} + 0.55$

	Sample spot	$\delta^{124/117}Sn_{3161A}$	$\delta^{124/117}Sn_{rod}$	2 SE	$\delta^{119/117}Sn_{rod}$	2 SE
1	17XL0501	0.30	–0.25	0.06	–0.09	0.03
2	17XL0502	0.38	–0.17	0.06	–0.06	0.03
3	17XL0503	0.20	–0.35	0.06	–0.11	0.03
4	17XL0504	0.20	–0.35	0.06	–0.12	0.03
5	17XL0505	–0.12	–0.67	0.06	–0.20	0.03
6	17XL0506	0.04	–0.51	0.06	–0.16	0.03
7	17XL0507	0.14	–0.41	0.06	–0.13	0.03
8	14XL0106	–0.14	–0.69	0.06	–0.21	0.04
9	14XL0105	–0.18	–0.73	0.06	–0.22	0.04
10	14XL0104	–0.17	–0.72	0.10	–0.21	0.07
11	14XL0102	–0.08	–0.63	0.08	–0.19	0.04
12	14XL0101	0.11	–0.44	0.08	–0.14	0.05
13	14XL0103	0.30	–0.25	0.08	–0.12	0.04

Results

The images of optical microscopy, cathodoluminescence (CL), and tantalum trace-element mapping of the two cassiterite crystals are presented in Figures 2e–2h and complemented by Online Materials[1] Figures OM2 and OM3. The complete list of LA trace-element data are in Online Materials[1] Tables OM1 and OM2. Some selected variation plots are in Figure 5 and will be discussed below. Additional variation plots are in Online Materials[1] Figure OM4.

The Sn isotope results of the two cassiterite crystals are presented in Table 1, relative to Sn rod = SPEX and also converted relative to NIST 3161 A. The slope of $\delta^{124/117}Sn$ vs. $\delta^{119/117}Sn$ is 3.6 with an $r^2 = 0.97$, very close to the terrestrial fractionation line with the slope of 3.5, indicating natural mass-dependent fractionation (Fig. 3). The 13 spot analyses on the two cassiterite crystals gave $\delta^{124/117}Sn_{3161A}$ values varying from –0.18 ± 0.06 to +0.38 ± 0.06‰ (2 SE). Figure 4 correlates the $\delta^{124/117}Sn$ data with the spot location relative to the crystal cross sections in Figures 2e–2f.

Discussion

Relationships between CL and trace-element zoning

The two cassiterite crystals have different zoning features, best visible in CL (Fig. 2): Sample 17XL05 displays a dark core zone and a mantle zone with oscillatory zoning between dominantly light zones, surrounded by a rim zone with two darker gray bands. Sample 14XL01 has a dark to medium gray core zone and a rim zone with very fine-grained muscovite inclusions, which produce a sieve pattern of minute dark domains (muscovite) and minute light gray domains (cassiterite) (Fig. 2d). This latter fabric could be related to co-precipitation of muscovite and cassiterite as deduced from the optical image.

Sample 17XL05 displays negative correlations between Sn vs. Ti and Sn vs. Fe (Online Materials[1] Figs. OM4a and OM4b), and positive correlations between U vs. Ti, Ta vs. Nb, and V vs. Sc (Fig. 5c; Online Materials[1] Figs. OM4c and OM4d). These correlations likely result from the various known ionic substitutions in the cassiterite structure, i.e., Ti^{4+}, Zr^{4+}, $U^{4+} \rightarrow Sn^{4+}$, $V^{5+} + Sc^{3+} \rightarrow 2Sn^{4+}$, $Fe^{3+} + (Nb, Ta)^{5+} \rightarrow 2Sn^{4+}$, $2(Nb, Ta)^{5+} + (Fe, Mn)^{2+} \rightarrow 3Sn^{4+}$ (Möller et al. 1988; Plimer et al. 1991; Murciego et al. 1997; Neiva 2008), and will not be further discussed here. The relationship of trace elements and CL features in cassiterite was discussed in Farmer et al. (1991).

The Ta contents are all below <1000 ppm and indicate a hydrothermal environment, whereas Ta >1000 pm, and up to

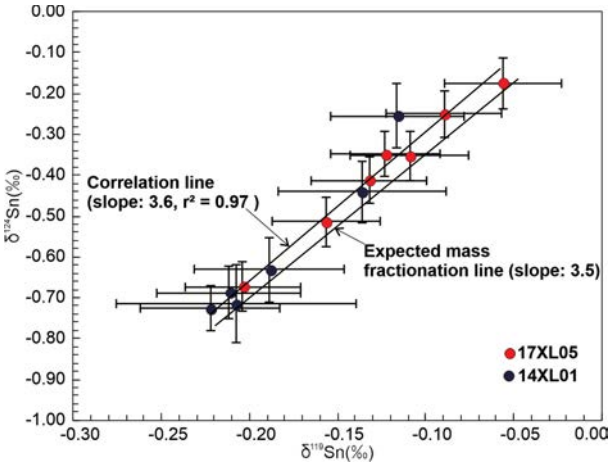

Figure 3. Mass dependence of the cassiterite Sn-isotope data. (Color online.)

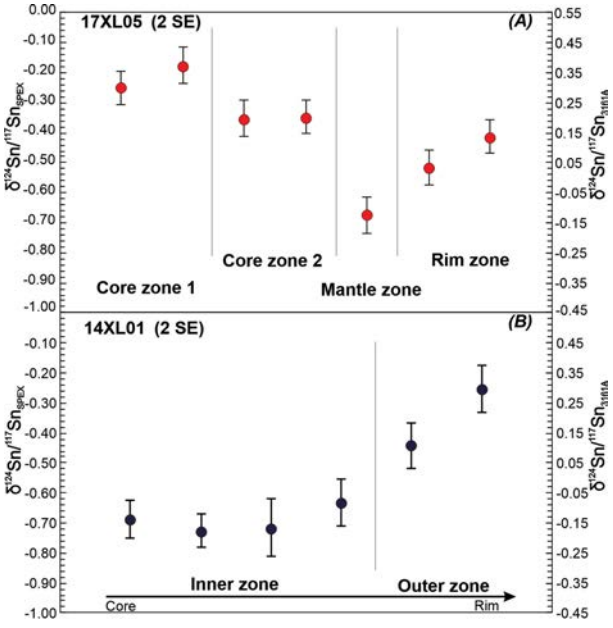

Figure 4. Sn isotope variation of the two cassiterite crystals, determined in situ by fs-LA-MC-ICP-MS, shown as $\delta^{124/117}Sn_{rod}$ relative to the bracketing standard Sn rod, which is indistinguishable to SPEX CLSN2-2Y (left y axis) and also as $\delta^{124/117}Sn_{3161A}$ relative to the NIST 3161A standard (right y axis, see text for details in conversion of the standards). Error bars are 2 SE. (Color online.)

the percent range, characterizes cassiterite from the transitional magmatic-hydrothermal stage, such as in rare-metal alkali-feldspar granite (Zoheir et al. 2020) or from rare-metal pegmatites (Tindle and Breaks 1998). Tantalum is largely insoluble in hydrothermal fluids, which is why Ta deposits are all related to rare-metal pegmatite systems but not to hydrothermal systems. Nevertheless, hydrothermal cassiterite carries Ta as a trace element, which likely is controlled by fluid conditions (temperature and composition) (Fesser 1968; Schneider et al. 1978; Tindle

and Breaks 1998; Lukyanova et al. 2017; Akinfiev et al. 2020). Zirconium is also an element largely immobile in acid fluid systems such as in tin ore systems and can be regarded as an indicator of fluid evolution, similar to Ta (Möller and Dulski 1983; Lehmann 1990). There are distinct differences between the two crystals studied, with consistent trends (Fig. 5). Sample 17XL05 has a core with elevated Ta (mean around 90 ppm Ta), which decreases outward rapidly down to about 1 ppm Ta in the mantle zone, while the rim zone is again rich in tantalum (mean around 167 ppm Ta). Sample 14XL01 has a core with very little Ta (≤1 ppm), and rim zone slightly elevated with 4–17 ppm Ta. These trends are also seen in zirconium, where the core of sample 17XL05 is again high (about 210 ppm Zr), the mantle zone is lower at about 90 ppm (mean) Zr, and the rim zone again higher with around 210 ppm Zr. Sample 14XL01 has a core with only about 1 ppm Zr and rim zone with slightly elevated Zr (mean around 15 ppm). The pattern of both elements can be understood as controlled by temperature and fluid composition/evolution. The lower Ta and Zr contents in the core zone of sample 14XL01 are likely related to a lower formation temperature of this cassiterite crystal in the muscovite vein stage and a corresponding change in fluid composition toward lower salinity. The overall elevated Ta and Zr contents in the core zone of sample 17XL05 are related to the higher temperature of formation in the feldspar stage and elevated salinity (and possibly also fluoride activity, which has a large control of Ta solubility; Akinfiev et al. 2020). The internal decrease in Zr and Ta in the mantle zone of this crystal indicates depletion of these two elements in a closed system. Interestingly, the rim zones in both crystals show again an increase in Ta and Zr, which suggests another fluid batch at elevated temperature. We will show below that these trends correlate with the Sn isotope patterns.

Insights from in situ Sn isotopes of cassiterite

The range of isotope ratios measured in the cassiterite crystals from Xiling, ~–0.1 to ~+0.4‰ $\delta^{124/117}Sn_{3161A}$, is within the 5‰ range reported for cassiterite samples worldwide, such as those given in Yao et al. (2018) for the major tin provinces (Cornwall, Erzgebirge, Bolivia), and St. Austell, Cornwall; Bangka, Indonesia; and Viloco, Bolivia (Schulze et al. 2017). The available data from South China correspond to the Xiling cassiterite, i.e., $\delta^{124/117}Sn_{3161A}$ for Dulong at –0.22 ± 0.18‰ (2 S.D.) and Gejiu at +0.22 ± 0.19‰ (2 S.D.), recalculated from the original $\delta^{124/120}Sn_{SPEX}$ data (Yamazaki et al. 2013). Overall, these data are close to bulk silicate earth of 0 to +0.2‰ $\delta^{124/117}Sn_{3161A}$ as estimated by Wang et al. (2018) and suggest little fractionation during the igneous formation and granite-related evolution of the magmatic-hydrothermal tin ore systems. However, the available data indicate significant differences between different tin deposits and within these deposits. The microanalytical in situ data of single cassiterite crystals indicate isotope fractionation processes within the hydrothermal (micro)-environment.

Seven spot analyses on cassiterite 17XL05 show $\delta^{124/117}Sn_{3161A}$ values varying from –0.12 ± 0.06 to +0.30 ± 0.06‰ (2 SE) (Fig. 4a). There is a narrow range of $\delta^{124/117}Sn$ (+0.20 to +0.38‰) values in the core zone with a little decrease from the core zone 1 to 2 (Fig. 4a). This decrease correlates with a significant decrease in Ta content from ~100 to ~10 ppm (Fig. 6). There is a distinct decrease from +0.20 to –12‰ $\delta^{124/117}Sn_{3161A}$ from the core to mantle zone (Fig. 4a). The mantle zone has very little Ta on the order of <2 ppm. Thus, the variation of $\delta^{124/117}Sn$ toward lighter Sn from the core to the mantle zones seems to correlate with a systematic decrease in Ta. Both trends can be interpreted as fluid evolution due to fractional crystallization with D (crystal/fluid) Ta ≫ 1, and preferential incorporation of heavy Sn isotopes into cassiterite.

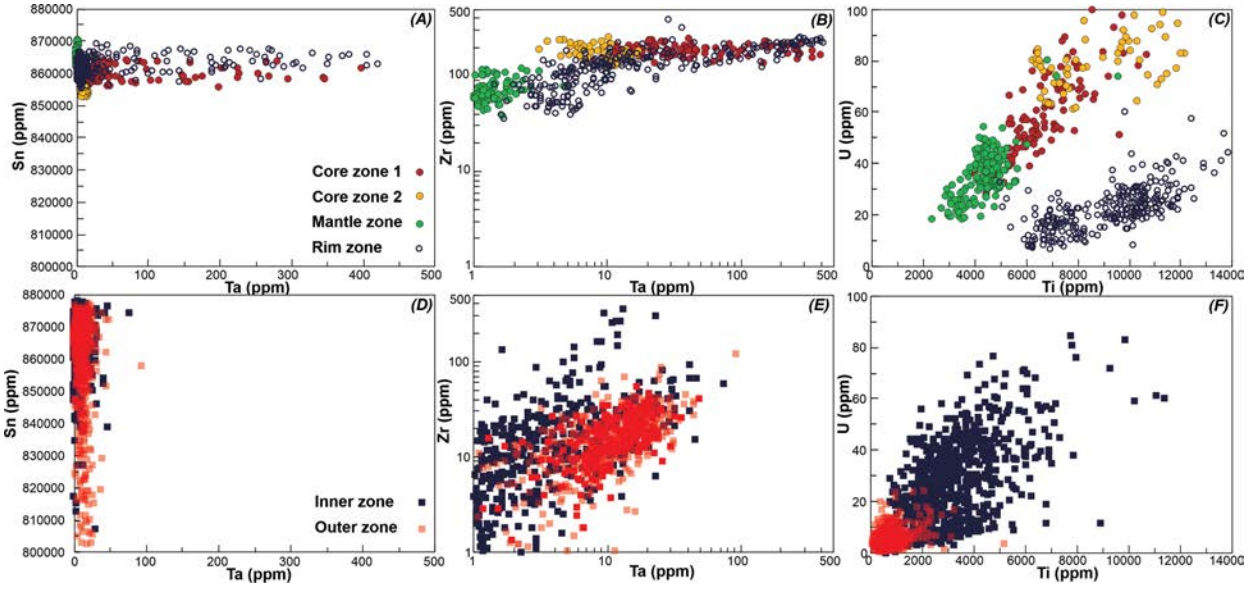

Figure 5. Selected scatterplots of trace elements (LA-ICP-MS) in the two cassiterite samples (upper row: Sample 17XL05; lower row: Sample 14XL01): (**a**, **b**, and **c**) Sn vs. Ta, Zr vs. Ta, and U vs. Ti plots of Sample 17XL05. (**d**, **e**, and **f**) Sn vs. Ta, Zr vs. Ta, and U vs. Ti plots of Sample 14XL01. The large range in Sn content in **d** is largely due to muscovite micro-inclusions. Overall elevated Ta and Zr contents in sample 17XL05 are due to the higher temperature of formation of this cassiterite crystal (**b**). This explanation also applies to the Ti-U plots (**c** and **f**), where the ratio of Ti/U in the fluid for the rim zone is apparently higher than for the core-mantle zones. (Color online.)

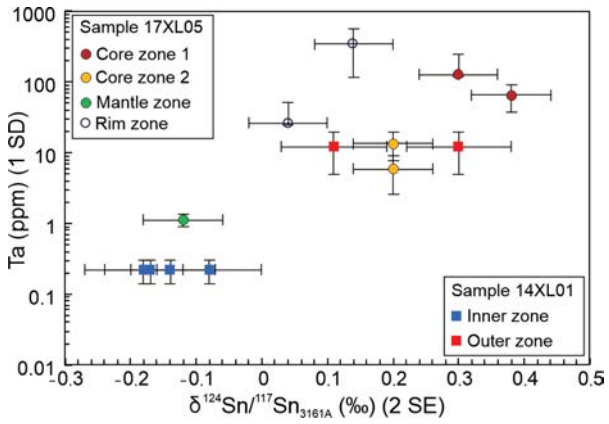

Figure 6. Correlation between $\delta^{124/117}Sn_{3161A}$ and Ta content (spot analysis) for the two cassiterite crystals analyzed. (Color online.)

Alternatively, Sn isotopes could fractionate during vapor-liquid phase separation (Wang et al. 2019b; She et al. 2020). However, in the case of Xiling, no low-salinity vapor fluid inclusions are observed, thus precluding the possibility of Sn transport as gaseous species. Also, with respect to Ta, Xiling has no individual Ta minerals, as expected according to the very low solubility of tantalum in aqueous fluids, and Ta is essentially in high-temperature cassiterite. In fact, cassiterite is the only tin mineral phase in the deposit sampled, and there is no stannite, which is known from other deposits to have lighter Sn compared to cassiterite. The latter characteristic has been explained as a result of redox-controlled Sn isotope fractionation, where heavy Sn is favored in cassiterite during the oxidation from Sn^{2+} (fluid) to Sn^{4+} (cassiterite), which then shifts the remaining fluid toward lighter composition in stannite (Yao et al. 2018). However, the same process can also explain the trend of lighter Sn composition in a single cassiterite crystal in a closed system (Polyakov et al. 2005).

Six spot analyses on cassiterite 14XL01 yield $\delta^{124/117}Sn_{3161A}$ values ranging from –0.17 ± 0.10 to +0.30 ± 0.08‰ (2 SE) (Fig. 4b). The four lower $\delta^{124/117}$Sn values in the inner zone are relatively uniform (–0.17 to –0.08‰), whereas the two $\delta^{124/117}$Sn values in the outer zone are higher and increase from +0.11 to +0.30‰ (Fig. 4b). The $\delta^{124/117}$Sn in the inner zone is similar to the mantle zone in sample 17XL05, whereas the Ta content is on the order of <1 ppm Ta. We interpret this situation as representing an advanced fluid evolution with respect to the Sn isotope composition and Ta content. The outer zone of crystal 14XL01 is characterized by very-fine-grained intergrowth of cassiterite and muscovite, as evidenced by sporadically elevated contents in Al (or deficiency in Sn) measured via LA-ICP-MS. The cassiterite has very variable but elevated Ta contents (Fig. 2h), and the isotope data characterize a less-evolved fluid compared to the inner zone (Fig. 6). Therefore, the rim zone must relate to a second fluid batch with an isotope composition similar to the initial fluid (core zone I) of crystal 17XL05 but of lower temperature as deduced from the relatively lower Ta and Zr contents.

Implications

Trace element compositions in cassiterite have been frequently used to fingerprint the fluid evolution of tin deposits. The new microanalytical technique of tin isotope tracing within individual cassiterite crystals provides an additional means to better characterize the multi-stage scenarios leading to tin ore formation. The single-spot tin isotope analysis documents tin isotope fractionation trends and yields information of the fluid system at high spatial (and by analogy: temporal) resolution. The in situ Sn isotope results reveal variations of Sn isotope composition through growth zones of single cassiterite crystals, which cannot be retrieved from conventional, solution Sn-isotope analysis of bulk samples. The isotopic trends in individual crystals show the interplay of fractional crystallization of the tin isotope composition in both closed- and open-fluid systems. Hence, tin isotope patterns in combination with trace-element microanalysis may help to better understand the complex zoning patterns of cassiterite and its associated fluid evolution.

Acknowledgments

Peng Liu thanks Alexandre Raphael Cabral, Wenlei Song, and Chao Zhao for editorial comments on an early version of this paper. We also thank Fangzhen Teng and Hongwu Xu, and two anonymous reviewers for their corrections and constructive comments.

Funding

This research was jointly funded by the National Natural Science Foundation of China Projects (41902072, 41820104010), the China Geological Survey Project (DD20190166-2020-06), Outstanding Chinese and Foreign Youth Exchange Program of China Association of Science and Technology (Peng Liu), and Fundamental Research Funds for the Central Universities (300102279301, 300102279401).

References cited

Akinfiev, N.N., Korzhinskaya, V.S., Kotova, N.P., Redkin, A.F., and Zotov, A.V. (2020) Niobiumn and tantalum in hydrothermal fluids: Thermodynamic description of hydroxide and hydroxofluoride complexes. Geochimica et Cosmochimica Acta, 280, 102–115.

Brügmann, G., Berger, D., and Pernicka, E. (2017) Determination of the tin stable isotopic composition in tin-bearing metals and minerals by MC-ICP-MS. Geostandards and Geoanalytical Research, 41, 437–448.

Chen, X.H., Hu, X.Z., and Cong, X.D. (1986) Genesis and mineralization of subgranitic porphyry, Xiling tin deposit, Guangdong. Geochimica, 1, 50–57 (in Chinese with English abstract).

Cheng, Y., Spandler, C., Kemp, A., Mao, J., Rusk, B., Hu, Y., and Blake, K. (2019) Controls on cassiterite (SnO_2) crystallization: Evidence from cathodoluminescence trace-element chemistry, and geochronology at the Gejiu tin district. American Mineralogist, 104, 118–129.

Creech, J.B., and Moynier, F. (2019) Tin and zinc stable isotope characterization of chondrites and implications for early Solar System evolution. Chemical Geology, 511, 81–90.

Farmer, C.B., Searl, A., and Halls, C. (1991) Cathodoluminescence and growth of cassiterite in the composite lodes at South Crofty Mine. Mineralogical Magazine, 55, 447–458.

Fesser, H. (1968) Spurenelemente in bolivianischen Zinnsteinen. Geologisches Jahrbuch, 85, 605–610.

Gilder, S., and Courtillot, V. (1997) Timing of the North-South China collision from new middle to late Mesozoic paleomagnetic data from the North China block. Journal of Geophysical Research, 102, 713–727.

Haustein, M., Gillis, C., and Pernicka, E. (2010) Tin isotopy-a new method for solving old questions. Archaeometry, 52, 816–832.

Heinrich, C.A. (1990) The chemistry of hydrothermal tin (tungsten) ore deposition. Economic Geology, 85, 457–481.

Horn, I., and von Blanckenburg, F. (2007) Investigation of elemental and isotopic fractionation during 196 nm femtosecond laser ablation multiple collector inductively coupled plasma mass spectrometry. Spectrochimica Acta Part B: Atomic Spectroscopy, 62, 410–422.

Jackson, K.J., and Helgeson, H.C. (1985a) Chemical and thermodynamic constraints on the hydrothermal transport and deposition of tin: I. Calculation of the solubility of cassiterite at high pressures and temperatures. Geochimica et Cosmochimica Acta, 49, 1–22.

——— (1985b) Chemical and thermodynamic constraints on the hydrothermal transport and deposition of tin. II. Interpretation of phase relations in the Southeast Asian tin belt. Economic Geology, 80, 1365–1378.

Lehmann, B. (1990) Metallogeny of Tin. Springer, 211 p.

Liu, Y., Hu, Z., Gao, S., Günther, D., Xu, J., Gao, C., and Chen, H. (2008) In situ

analysis of major and trace elements of anhydrous minerals by LA-ICP-MS without applying an internal standard. Chemical Geology, 257, 34–43.
Liu, P., Mao, J.W., Cheng, Y.B., Yao, W., Wang, X.Y., and Hao, D. (2017) An early Cretaceous W-Sn deposit and its implications in southeast coastal metallogenic belt: Constraints from U-Pb, Re-Os, Ar-Ar geochronology at the Feie'shan W-Sn deposit, SE China. Ore Geology Reviews, 81, 112–122.
Liu, P., Mao, J.W., Santosh, M., Xu, L.G., Zhang, R.Q., and Jia, L.H. (2018) The Xiling Sn deposit, eastern Guangdong Province, Southeast China: A new genetic model from $^{40}Ar/^{39}Ar$ muscovite and U-Pb cassiterite and zircon geochronology. Economic Geology, 113, 511–530.
Liu, P., Mao, J.W., Jian, W., and Mathur, R. (2020) Fluid mixing leads to main-stage cassiterite precipitation at the Xiling Sn polymetallic deposit, SE China: Evidence from fluid inclusions and multiple stable isotopes (H-O-S). Mineralium Deposita, 55, 1233–1246.
Lukyanova, E.V., Akinfiev, N.N., Zotov, A.V., Rass, I.T., Kotova, N.P., and Korzhinskaya, V.S. (2017) Niobium in hydrothermal systems related to alkali granites: Thermodynamic description of hydroxide and hydroxofluoride complexes. Geology of Ore Deposits, 59, 305–314.
Mao, J.W., Xie, G.Q., and Guo, C.L. (2007) Large-scale tungsten mineralization in the Nanling region, south China: Metallogenic ages and corresponding geodynamic processes. Acta Petrologica Sinica, 23, 2329–2338 (in Chinese with English abstract).
Möller, P., and Dulski, P. (1983) Fractionation of Zr and Hf in cassiterite. Chemical Geology, 40, 1–12.
Möller, P., Dulski, P., Szacki, W., Malow, G., and Riedel, E. (1988) Substitution of tin in cassiterite by tantalum, niobium, tungsten, iron and manganese. Geochimica et Cosmochimica Acta, 52, 1497–1503.
Murciego, A., Sanchez, A.G., Dusausoy, Y., Pozas, J.M., and Ruck, R. (1997) Geochemistry and EPR of cassiterite from the Iberian Hercynian Massif. Mineralogical Magazine, 61, 357–365.
Neiva, A.M.R. (2008) Geochemistry of cassiterite and wolframite from tin and tungsten quartz veins in Portugal. Ore Geology Reviews, 33, 221–238.
Plimer, I.R., Lu, J., and Kleeman, J.D. (1991) Trace and rare earth elements in cassiterite-sources of components for the tin deposits of the Mole Granite. Mineralium Deposita, 26, 267–274.
Polyakov, V.B., Mineev, S.D., Clayton, R.N., Hu, G., and Mineev, K.S. (2005) Determination of tin equilibrium isotope fractionation factors from synchrotron radiation experiments. Geochimica et Cosmochimica Acta, 69, 5531–5536.
Schneider, H.-J., Dulski, P., Luck, J., Möller, P., and Villalpando, A. (1978) Correlation of trace element distribution in cassiterites and geotectonic position of their deposits in Bolivia. Mineralium Deposita, 13, 119–122.
Schulze, M., Ziegerick, M., Horn, I., Weyer, S., and Vogt, C. (2017) Determination of tin isotope ratios in cassiterite by femtosecond laser ablation multicollector inductively coupled plasma mass spectrometry. Spectrochimica Acta Part B: Atomic Spectroscopy, 130, 26–34.
She, J.X., Wang, T.H., Liang, H.D., Muhtar, M.N., Li, W.Q., and Liu, X.D. (2020) Sn isotope fractionation during volatilization of Sn (IV) chloride: Laboratory experiments and quantum mechanical calculations. Geochimica et Cosmochimica Acta, 269, 184–202.
Tindle, A.G., and Breaks, F.W. (1998) Oxide minerals of the Separation Rapids rare-element granitic pegmatite group, northwestern Ontario. Canadian Mineralogist, 36, 609–635.
Wang, F.Y., Ge, C., Ning, S.Y., Nie, L.Q., Zhong, G.X., and White, N.C. (2017) A new approach to LA–ICP–MS mapping and application in Geology. Acta Petrologica Sinica, 33, 3422–3426 (in Chinese with English abstract).
Wang, X., Amet, Q., Fitoussi, C., and Bourdon, B. (2018) Tin isotope fractionation during magmatic processes and the isotope composition of the bulk silicate Earth. Geochimica et Cosmochimica Acta, 228, 320–335.
Wang, X.Y., Fitoussi, C., Bourdon, B., Fegley, B., and Charnoz, S. (2019a) Tin isotopes indicative of liquid-vapour equilibration and separation in the Moon-forming disk. Nature Geoscience, 12, 707–1019.
Wang, D., Mathur, R., Powel, W., Godfrey, L., and Zheng, Y.Y. (2019b) Experimental evidence for fractionation of tin chlorides by redox and vapor mechanism. Geochimica et Cosmochimica Acta, 250, 209–218.
Yamazaki, E., Nakai, S.I., Yokoyama, T., Ishihara, S., and Tang, H.F. (2013) Tin isotope analysis of cassiterites from Southeastern and Eastern Asia. Geochemical Journal, 47, 21–35.
Yao, J.M., Mathur, R., Powell, W., Lehmann, B., Tornos, F., Wilson, M., and Ruiz, J. (2018) Sn-isotope fractionation as a record of hydrothermal redox reactions. American Mineralogist, 103, 1591–1598.
Yuan, S.D., Peng, J.T., Hu, R.Z., Li, H.M., Shen, N.P., and Zhang, D.L. (2008) A precise U–Pb age of cassiterite from the Xianghualing tin–polymetallic deposit (Hunan, South China). Mineralium Deposita, 43, 375–382.
Zoheir, B., Lehmann, B., Emam, A., Radwan, A., Zhang, R., Bain, W.M., Steele-MacInnis, M., and Nolte, N. (2020) Extreme fractionation and magmatic-hydrothermal transition in the formation of Abu Dabbab rare-metal granite, Eastern Desert, Egypt. Lithos, 352-353, 105329.

Manuscript received April, 10 2020
Manuscript accepted December 29, 2020
Manuscript handled by Fang-Zhen Teng

Endnote:

[1]Deposit item AM-21-127558, Online Materials. Deposit items are free to all readers and found on the MSA website, via the specific issue's Table of Contents (go to http://www.minsocam.org/MSA/AmMin/TOC/2021/Dec2021_data/Dec2021_data.html).